SUPPORTING INFORMATION

Charge trapping and de-trapping in isolated CdSe/ZnS nanocrystals under an external electric field: indirect evidence for a permanent dipole moment

[1]Huidong Zang, [2]Mihail Cristea,[1] Xuan Shen,[1]Mingzhao Liu, [1]Fernando Camino and [1,*]Mircea Cotlet

[1]Center for Functional Nanomaterials, Brookhaven National Laboratory, Upton NY 11973, USA and [2]Physics Department, University "Politehnica" of Bucharest, 313 Splaiul Independentei, Bucharest RO-060042, Romania

1. Materials and Device fabrication

Qdot 605 ITK organic quantum dots (in toluene) and PMMA were purchased from Life Technologies Inc. and Sigma Aldrich Inc., respectively. The QDs were sandwiched between two planar electrodes with architecture as ITO/SiO2/QDs/PMMA/Al. First, a 200 nm thin SiO2 insulating layer was grown on ITO glass (SPI Supplies Inc.) by Plasma Enhanced Chemical Vapor Deposition (PECVD) method, then the QDs were diluted in toluene at 50 pM and spun coated on SiO2. A 200 nm thin layer of PMMA (dissolved in chloroform) was obtained by spin coating on top of the QDs covering the SiO2 and finally, a 100 nm thin aluminum (Al) layer was deposited on PMMA through thermal evaporation under a vacuum

of 7×10-7Torr. The dielectric constant for SiO2 and PMMA are both around 3.9[1, 2]such that boundary conditions can be neglected. The density of the QDs on SiO2 was less than one QD/μm2. An electric field was applied using a Keithley 2635 source meter programmed in Labview.

2. Time-resolved Confocal Photoluminescence Microscopy

Time resolved confocal PL microscopy was performed on a home-built confocal scanning stage microscope based on an inverted microscope (Olympus IX81, 1.4 NA 100× oil objective) equipped with a piezo scanning stage (Physik Instrumente, Germany) and coupled to a diode-pumped solid-state laser system (Picoquant, Germany) delivering 440 nm at 10 MHz repetition rate. The average power at the sample was kept at 300 nW. Photoluminescence was collected by the same objective lens, filtered from laser excitation by a dichroic mirror (Semrock, DiO-532) and by a band-pass filter (FF01-605/50, Semrock), spatially filtered by a pinhole (75 μm) and detected by a single photon counting avalanche photodiode (SPAD MPD PicoQuant). The signal generated onto the SPAD was fed into a time analyzer (PicoHarp 300, PicoQuant) and detected in time-tag time-resolved (TTTR) mode, which allowed fluorescence lifetime imaging and probing of isolated QDs. Each isolated QD was probed for 60 seconds by recording both the PL intensity and PL lifetime, with data acquisition and analysis performed with Symphotime 32 Picoquant software. PL lifetimes reported in Fig. 3c&f were estimated from PL decays histogrammed with a resolution of 8 ps/bin. Lifetimes were obtained from bi-exponential fits as amplitude averaged lifetimes by using the FluoFit Picoquant Software with reported errors calculated with the Support Plane Analysis procedure implemented in Fluofit. PL lifetimes reported in Fig.2b&c and Fig.4 were calculated using a constant time (117 ms interval) sliding procedure, with each PL decay rebinned to 64 ps/bin and fit by a single exponential model using a Maximum

Likelihood Estimator procedure. For two-color detection experiments employed to generate Figure 6, main text, we used a 605nm dichroic (Semrock) to separate the PL from isolated QDs onto blue and red spectral bands that were each detected by identical single photon counting detectors, with the mentioning that the emission of these QDs peaks at 605nm. Photon pair correlation (antibunching) experiments were performed using a classical Hanbury-Twiss and Brown type experiment in combination with pulsed excitation (e.g. 440nm, 10 MHz) by using a 50/50 non-polarizing beam splitter to split the PL signal from isolated QDs onto two identical SPADs whose signals were fed onto a time analyzer (SPC850 Becker&Hickl, Germany). A histogram of interphoton arrival times lacking a peak at zero time, as shown in Figure S1, is a confirmation of the detection of isolated QDs.

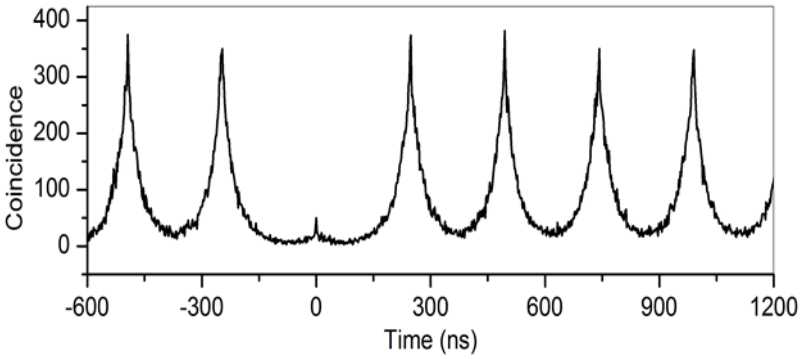

Figure S1. Photon antibunching curve for a single CdSe/ZnS QD in device under zero electrical bias.

3. Calculation on $P_{on}(t)$ and $P_{off}(t)$ probabilities.

Probability densities $P_{on}(t)$ and $P_{off}(t)$ were calculated according to a previously published method[3-5]

$$P_i(t) = \frac{N_i}{N_{i,total}} \times \frac{1}{\Delta t_{avg}} (i = on\ or\ off) \qquad (1)$$

with N_i representing the number of *on* (*off*) events with duration time *t*, $N_{i,total}$ the total number of *on* (*off*) events, and Δt_{avg} the average duration time between nearest neighbor event. Separation of *on* and *off* events was done using a threshold equal to the standard deviation of the PL intensity above the mean value of the background signal[6] using PL intensity traces binned at 1 ms.

4. Calculation on $P_{on}(t)$ and $P_{off}(t)$ probabilities with different bin time

It has been reported that changing the bin time will change the blinking parameters.[7] Here we did $P_{on}(t)$ and $P_{off}(t)$ probabilities calculation for the Figure 3d in main text with 1ms and 10ms bin time. It is found that changing the bin time did change the value of the fitted parameters; however, it will not change the trend (see Figure S2a-d). So this confirms that the experimental results we found are not due to the artifact of data processing.

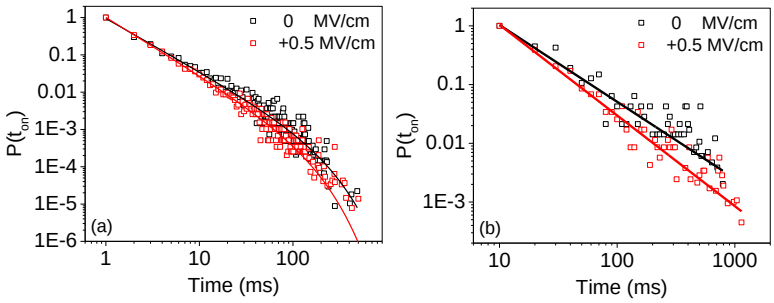

Figure S2. $P_{on}(t)$ probabilities for the PL intensity trajectories in Figure 3d in main text. Figure S2a and Figure S2b are at bin time with 1ms and 10ms, respectively. The solid lines are the fit and the fitted values are in table S1.

Bin time	External bias (MV/cm)	m_{on}	$\Delta m_{on}=m_{on}(0)-m_{on}(E)$
1ms	0	1.42	-0.12
	+0.5	1.54	
10ms	0	1.31	-0.23
	+0.5	1.54	

5. Calculation of PL spectral peak shift by QCSE.

Using the PL intensity ratio data from Fig.6c and the predicted PL intensity ratio change vs wavelength shown in Fig.S3, a dependency PL emission peak vs external electric field was obtained and shown in Fig.6h, main text.

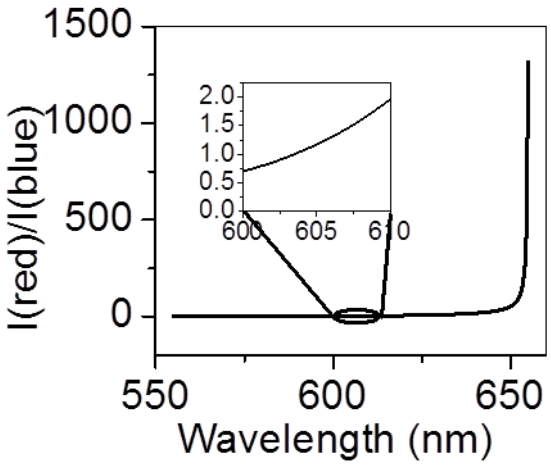

Figure S3. PL intensity ratio, I(red)/I(blue) vs PL peak position calculated from the PL spectrum in Fig.6g, main text. Inset is a zoom

6. High resolution transmission electron microscopy and QD size distribution

High resolution transmission electron microscopy (HRTEM) was used to examine the crystal structure of CdSe nanoparticles. Figure S4a indicates typical hexagonal close packed structure of [001] zone axes. The Fast Fourier Transform (FFT) image is also shown in the inset with six-fold hexagonal symmetric structure. However, it is still not enough to exclude the zinc-blende structure, since the hexagonal symmetric structure can be also observed via [111] zone axes of cubic structure. So we recorded the selected area electron diffraction (SAED) ring patterns as displayed in Figure S4b. By carefully comparing the standard diffraction ring patterns, the CdSe nanoparticles could be indexed to the Wurtzite structure, because the reciprocal spacing of 3.8 nm^{-1} can be only observed in this structure. It also should be noticed that the diffraction ring indicated by dashed line is from the shell material of ZnS.

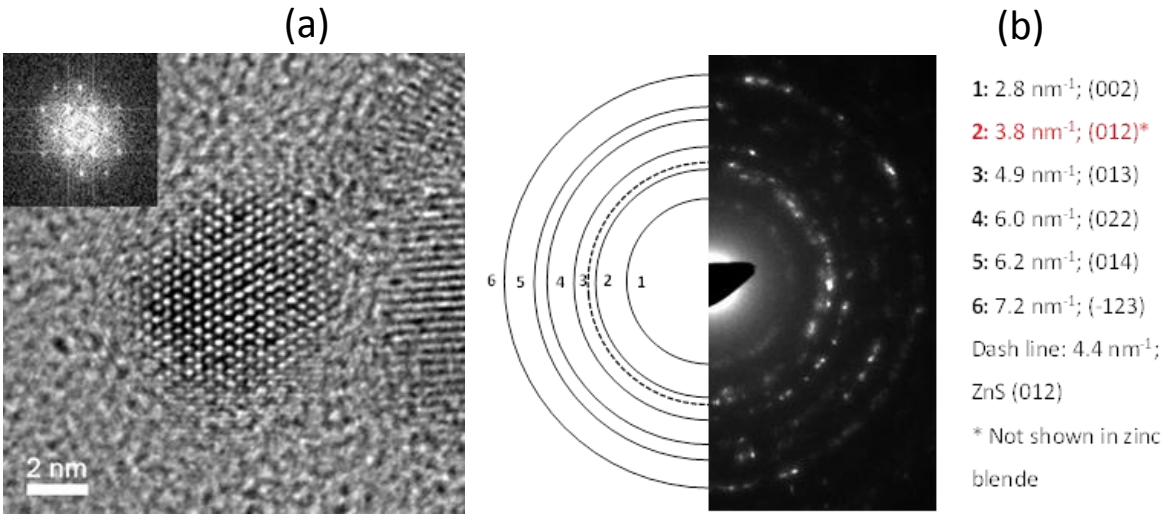

Figure S4. (a) HRTEM and FFT (insert figure) images for single CdSe/ZnS QD. (b) SAED ring patterns of the CdSe/ZnS QD, dashed ring at 4.4 nm^{-1} is from shell ZnS.

The TEM image of CdSe/ZnS QDs is shown in Figure S5a, the histogram of the size distribution is shown in Figure S5b, the black line is a Gaussian fit for the histogram with peak value 7.5nm. The core size of 4.4nm was estimated by comparing the first absorption

peak of the QDs (data not shown) with the data reported in[8] . Therefore, a shell thickness of 1.5-1.6nm was estimated based on Fig.S5b.

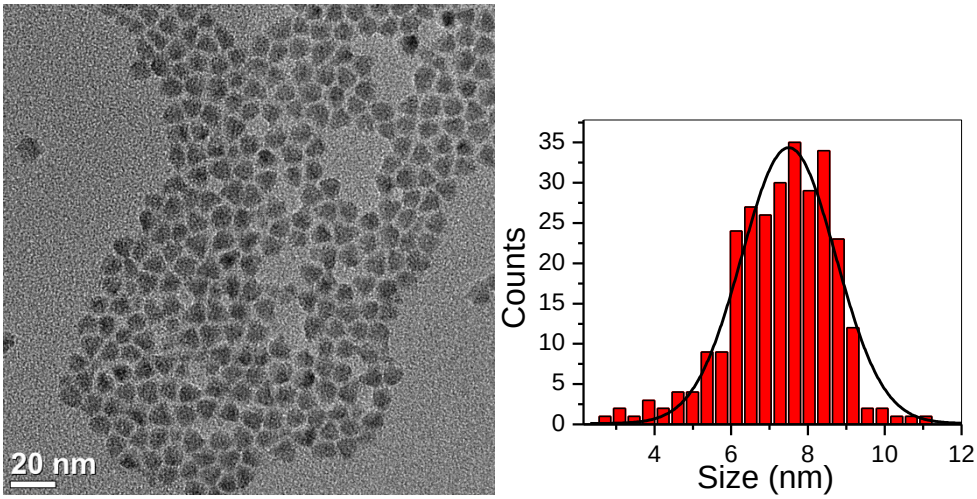

Figure S5. (a) TEM image for single CdSe/ZnS QD. (b) Size distribution of the CdSe/ZnS QDs shown in figure S5a, the black line is a Gaussian fit for the histogram.

7. Theoretical calculation of probability density of electron and hole in QD.

The interaction between electron and hole confined in a QD is described by a Hamiltonian

$$\hat{H} = \hat{H}_e + \hat{H}_h - \frac{q^2}{4\pi\varepsilon|\vec{r}_e - \vec{r}_h|}, \qquad (2)$$

where $\hat{H}_e$ and $\hat{H}_h$ represent the single particle Hamilton operator for electron and hole, respectively. The last term represents the Coulomb interaction between electron and hole, $\vec{r}_e$. and $\vec{r}_h$ being the electron and hole position vectors. The average value of the Coulomb interaction can be evaluated if knowing the single particle wave functions (WFs), and the overlap integral of WFs is strongly reduced by either the electric field or by the permanent dipole moment.

The single-particle Schrodinger equation with the Hamiltonian is given by

$$\hat{H}_{e,h} = -\frac{\hbar^2}{2m^*_{e,h}}\nabla^2 + V_{0e,h} - q\vec{E}\cdot\vec{z} - \frac{\vec{\mu}\cdot\vec{r}q}{4\pi\varepsilon_0\varepsilon_r r^3} \quad (3)$$

and it can be solved by 3D Finite Element Method (FEM) with triangular elements. Here index 'e' refers to the electron in conduction band (CB), and 'h' refers to the heavy-hole in valence band (VB).

Calculations were performed by using a specialized eigenvalue problem software with nonlinear solver. The solution accuracy was increased by restarting the numerical procedure using as initial values the solution obtained earlier. The domain discretization is not uniform, the finite element size being much smaller in the region when the wave functions present a significant variation from one iteration to another one. The iteration is stopped when a fixed limit error is reached (0.001 meV). A wave function zero value (Dirichlet condition) was imposed at the shell surface and at the interface between core and shell. Continuity of wave function and of the first derivative were imposed. The values of the various physical parameters used in the calculations are given in table S2, and the dipole moment is 70D.[9]

Table S2. Parameters used in the numerical simulations.

Parameters	**CdSe**	**ZnS**
$E_g(eV)$	1.87	3.741
m_e^*/m_0	0.13	0.28
m_h^*/m_0	0.45	0.49
$\varepsilon/\varepsilon_0$	9.3	8.1
$V_e(eV)$	0	0.992

$V_h(eV)$	0	0.881

1. Gray, P. R., *Analysis and Design of Analog Integrated Circuits*. John Wiley & Sons, Incorporated: 2010.
2. Kuehn, S.; Loring, R. F.; Marohn, J. A. *Phys Rev Lett* **2006,** 96, (15), 156103.
3. Kuno, M.; Fromm, D. P.; Hamann, H. F.; Gallagher, A.; Nesbitt, D. J. *J Chem Phys* **2001,** 115, (2), 1028-1040.
4. Jin, S. Y.; Hsiang, J. C.; Zhu, H. M.; Song, N. H.; Dickson, R. M.; Lian, T. Q. *Chemical Science* **2010,** 1, (4), 519-526.
5. Song, N. H.; Zhu, H. M.; Jin, S. Y.; Zhan, W.; Lian, T. Q. *Acs Nano* **2011,** 5, (1), 613-621.
6. Kuno, M.; Fromm, D. P.; Hamann, H. F.; Gallagher, A.; Nesbitt, D. J. *J Chem Phys* **2000,** 112, (7), 3117-3120.
7. Crouch, C. H.; Sauter, O.; Wu, X.; Purcell, R.; Querner, C.; Drndic, M.; Pelton, M. *Nano Letters* **2010,** 10, (5), 1692-1698.
8. Yu, W. W.; Qu, L.; Guo, W.; Peng, X. *Chem Mater* **2003,** 15, (14), 2854-2860.
9. Shim, M.; Guyot-Sionnest, P. *The Journal of Chemical Physics* **1999,** 111, (15), 6955-6964.